Research Article | Vol. 12, No. 2 / 1 February 2021 / Biomedical Optics Express 1105

Biomedical Optics EXPRESS

In vivo test-driven upgrade of a time domain multi-wavelength optical mammograph

GIULIA MAFFEIS,[1,*] EDOARDO FEROCINO,[1] ALBERTO DALLA MORA,[1] ANTONIO PIFFERI,[1,2] RINALDO CUBEDDU,[1] AND PAOLA TARONI[1,2]

[1] *Politecnico di Milano, Department of Physics, Piazza Leonardo da Vinci, 32, 20133, Milan, Italy*
[2] *CNR-Istituto di Fotonica e Nanotecnologie, Piazza Leonardo da Vinci, 32, 20133, Milan, Italy*
[*] *giulia.maffeis@polimi.it*

Abstract: A recent upgrade of the time domain multi-wavelength optical mammograph developed by Politecnico di Milano achieved good performance in laboratory tests [Biomed. Opt. Express **9**, 755 (2018).]. However, it proved unsatisfactory when *in vivo* measurements were finally performed. That led to a further upgrade, including the replacement of the time-to-digital converter with a new model, and the related set-up changes. The new instrument version offers improved laboratory performance (as assessed through established protocols: BIP and MEDPHOT) and good *in vivo* performance (extension of the scanned breast area, repeatability, consistency of estimated tissue composition with physiology). Besides introducing the new set-up and detailing its laboratory and *in vivo* performance, we highlight the importance of systematic *in vivo* testing before entering clinical trials.

© 2021 Optical Society of America under the terms of the OSA Open Access Publishing Agreement

1. Introduction

Neoadjuvant chemotherapy (NAC) is more and more widespread to reduce tumor size before surgery and favor breast conserving lumpectomy [1]. Therapy monitoring is important in order to assess effectiveness and determine if any adjustments are needed. Now-a-days, the response to NAC is mainly monitored through magnetic resonance imaging (MRI) and positron emission tomography (PET) [2]. However, they are not recommended for frequent measurements especially due to high costs, long examination times, and the need of toxic contrast agents. X-ray mammography is not the preferred strategy for assessing response to NAC since it suffers from low sensitivity to therapy-induced changes and implies the use of ionizing radiation, which should be avoided when repeated exams are performed over a short period of time.

Non-invasiveness and sensitivity to changes in tissue composition and physiology are essential features for a monitoring technique. Diffuse optics, and in particular its application to breast imaging (*i.e.* optical mammography), could at least in principle address most of such clinical needs [3–6], exploiting light to probe tissue composition and microstructure, as well as blood parameters.

Several research groups have already obtained interesting results applying diffuse optics to monitor NAC, with different instrument architectures and implementations [7]. Some of them are cited in Table 1, where their key features are highlighted to show that differences exist in the experimental approach as well as in the information on tissue they retrieve.

The majority of the set-ups were based on (or exploited also) the Frequency Domain (FD) approach [3] and used PhotoMultiplier Tubes (PMTs) as detectors. Besides, hemoglobin was the main tissue constituent that most research groups focused on.

A different implementation of diffuse optics is based on the Time Domain (TD) approach [3]. In this framework, Taroni and coworkers from the Department of Physics at Politecnico di Milano have developed and upgraded over time a TD optical mammograph operating at

#412210 https://doi.org/10.1364/BOE.412210
Journal © 2021 Received 15 Oct 2020; revised 6 Jan 2021; accepted 19 Jan 2021; published 27 Jan 2021

Biomedical Optics EXPRESS

Table 1. Examples of studies about NAC monitoring with diffuse optics[a]

Group	Approach	Geometry	Detector	Chromophores	References
Tromberg	CW / FD	Reflectance	APD	HbO2, Hb, HbT, SO2, water, lipid	[13,14]
Zhu	FD	Reflectance	PMT	HbO2, Hb, HbT	[15,16]
Jiang	FD	Reflectance	PMT	HbO2, Hb, HbT, SO2, water	[17,18]
Carp	CW / FD	Transmittance	PMT / APD	HbO2, Hb, HbT, SO2	[19]
Hielscher	CW	Reflectance	PD	HbO2, Hb, water, lipid	[20,21]

[a]CW: Continuous Wave, FD: Frequency Domain, TD: Time Domain, APD: Avalanche PhotoDiode, PMT: PhotoMultiplier Tube, PD: PhotoDiode, HbO_2: Oxy-hemoglobin, Hb: Deoxy-hemoglobin, HbT: Total hemoglobin, SO_2: Oxygen Saturation.

multiple wavelengths over a broad spectral range. The instrument has already been employed in clinical trials in the past, with the goal of investigating optical mammography as a means for the assessment of breast density as a risk factor [8,9] and for the discrimination between malignant and benign lesions [10–12].

NAC monitoring is the new emerging application we wish to explore with optical mammography. For that purpose, we have recently realized a new implementation of our TD optical mammograph, exploiting the large harvesting and processing capability of Silicon PhotoMultiplier (SiPM)-based detection combined with parallel Time-to-Digital Conversion (TDC) acquisition, still preserving the wide spectral coverage (635–1060 nm) required to investigate multiple tissue absorbers [22]. The system was developed to enter a clinical study on the monitoring (and potentially the prediction) of tumor response to NAC through TD diffuse optics, with particular emphasis on the assessment of key tissue constituents other than hemoglobin, namely water, lipid and in particular collagen, which plays a major role in tumor onset and progression [23] and could prove to affect treatment and be a key biomarker of its efficacy [24,25]. Before entering the clinical study, we tested the Technology Readiness Level (TRL) of our instrument, following a methodology initially conceived at NASA to qualify space missions [26], and currently adopted in many contexts, including EU funding agencies, whose definition we follow here [27]. Taken for granted from previous studies and abundant literature, the first levels – *i.e.* TRL1 = "Basic principles observed", TRL2 = "Technology concept formulated", TRL3 = "Experimental proof of concept" – the system passed all basic tests in the laboratory to comply with TRL4 = "Technology validated in lab". By testing the system on healthy volunteers, in the path towards TRL5 = "Technology validated in relevant environment", which in our case means "clinical settings", we faced unexpected issues, related to inter- and intra-subject variability and to the specificities of the *in vivo* conditions – as detailed in Section 2.3. The system was thus upgraded, identifying new technologies that could better face the *in vivo*-related issues, and tested again following standard protocols (BIP [28] and MEDPHOT [29]) reaching TRL4 with better scores than the previous implementation. Further, in the following preliminary *in vivo* tests on volunteers towards TRL5, the key hurdles were all solved.

With this paper we wish to highlight the problems we encountered when passing from the lab to the *in vivo* environment, and the solutions we adopted, which can be useful to other groups working also on different applications (*e.g.*, brain imaging). Further, we wish to contribute to the formulation of good practices for the transition from TRL4 to TRL5. In the last two decades, extensive work has been devoted to identify the relevant steps to pass TRL4, leading, for instance, to three protocols for performance assessment of diffuse optics instruments (BIP, MEDPHOT, NEUROPT [28–30]) and to a large multi-laboratory exercise (BITMAP [31,32]), which involved 7 Institutions and 10 diffuse optics systems. Conversely, the achievement of TRL5 in diffuse optics applications is still largely subjective and lacks helpful guidelines, despite some remarkable efforts, such as the ACRIN 6691 trial on breast NAC [13] or the SafeBoosC II initiative on

Biomedical Optics EXPRESS

brain oxygenation monitoring in preterm babies [33]. Our work adds a small contribution in that direction, focusing on the steps needed to move from TRL4 to TRL5, by identifying some parameters and tests (*e.g.*, reproducibility in the quantification of tissue composition), which according to our experience proved decisive when moving from lab to *in vivo* conditions. The transition from TRL4 to TRL5 was also addressed by a recent workshop on "Performance Assessment and Standardization in Biophotonics" held at the European Commission premises, where a key conclusion was the need to anticipate as much as possible problems occurring in *in vivo* validation to the lab stage, before long, expensive and ethically delicate clinical studies are started [33]. This approach falls also in the direction of granting higher reliability, comparability and traceability of clinical datasets at the basis of the fascinating perspectives of Open Science.

2. Instrument set-ups and performance assessment methods

2.1. Initial instrument set-up

The instrumental set-up that had recently successfully passed the laboratory performance assessment [22] is briefly recalled for easier understanding of the following upgrades made to address problems emerged during the *in vivo* tests.

The optical mammograph operates at 7 wavelengths in the red and near-infrared range, in the time domain, in transmittance geometry, on a breast mildly compressed between plane parallel glass plates. The measurement acquisition geometry is similar to the one adopted for x-ray mammography, except for the fact that milder compression is applied and the patient is asked to sit in front of the compression unit for a comfortable examination, as it takes significantly longer (few minutes) than a conventional mammography. The compression unit can be rotated by angles of up to 90° in both clockwise and counter-clockwise direction, thus enabling the acquisition of images in the cranio-caudal (CC), medio-lateral or oblique (OB, 45°) views. Further details on the compression unit can be found in [34].

As shown in Fig. 1 (top), 7 picosecond pulsed diode lasers (LDH-P-XXX, PicoQuant, Germany, with XXX representing the nominal wavelength in nanometers) emitting at 635, 680, 785, 905, 930, 975 and 1060 nm are used as light sources, controlled by a single driver (PDL-828 "Sepia II", PicoQuant). Their repetition rate is 10 MHz and the average output power is in the range of 1–5 mW, depending on wavelength. Circular variable neutral density filters are placed on each of the illumination paths to tune the light power independently for each wavelength. The emitted pulses are properly delayed and then combined into a single injection fiber, resulting into a train of 7 laser pulses at 7 different wavelengths in a time window of 100 ns (*i.e.* the laser pulses are separated by about 14.3 ns). The fiber is followed by a lens producing a 5 mm-diameter collimated beam that illuminates the breast. The breast is raster-scanned by the injection fiber, which is axially aligned with a detection probe, composed of 8 SiPMs (S13360-1350PE, Hamamatsu Photonics, Japan) in a square pattern and moved synchronously with the injection fiber.

The scan is limited to the breast area, so as to save measurement time and disk space. Therefore, the scan range for both transverse and longitudinal directions depends on the breast size, with a maximum scan range of 24×18 cm^2. With this initial set-up, measurements were regularly performed every 1 mm along both transverse and longitudinal directions, for an acquisition time of 25 ms/mm. For each wavelength and SiPM, the initial count rate was fixed at 150000 counts per second. A complete scan usually required about 5 minutes, depending on the breast size. The output signals were properly amplified from few mV to few tens of mV, and then translated to Low-Voltage Transistor-Transistor Logic (LVTTL), as required by the Time-To-Digital Converter model (SC-TDC 1000/08 S, Surface Concept, Germany [35]) chosen to acquire the time-resolved transmittance curves.

As explained in [22], to provide proper photon-timing information the SC-TDC sync rate has to be kept well below 7 MHz. Since the laser master oscillator rate was 10 MHz, a native sync divider function (factor of 3) was exploited, thus resulting into the generation of 3 replicas of the

Biomedical Optics EXPRESS

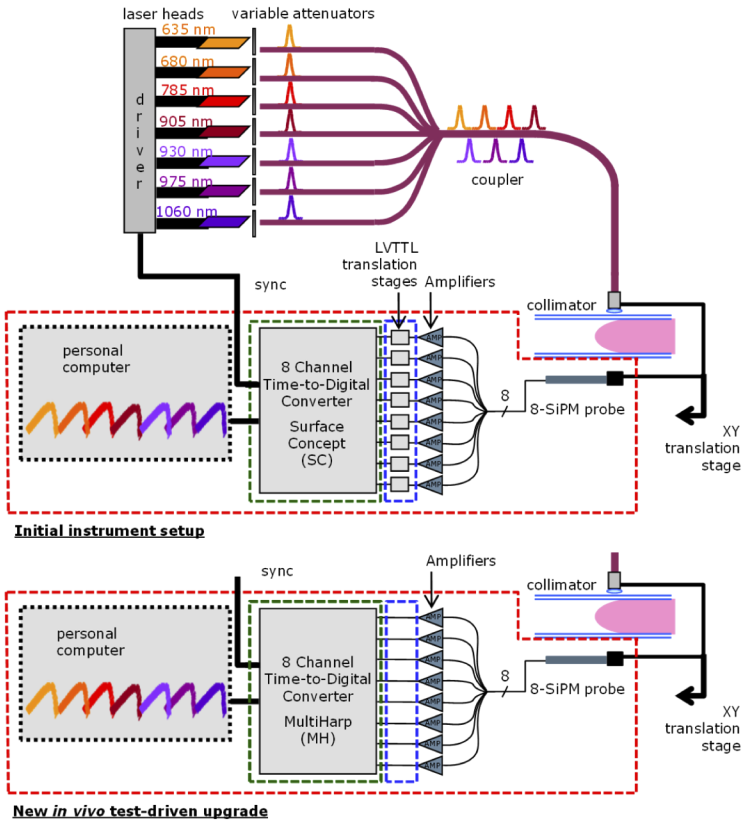

Fig. 1. Initial instrument set-up (top) and *in vivo* test-driven instrument upgrade concerning signal processing and acquisition electronics changed from SC-TDC to MH, (bottom).

7 Distributions of Time Of Flights (DTOFs) acquired due to the injection in the tissue of 7 laser pulses at different wavelengths every 100 ns. The overall time scale of the SC-TDC was therefore $3 \cdot 100$ ns. To allow proper data analysis, the 3 DTOF replicas at the same wavelengths had to be superposed in post-processing, thus summing up all the available information into a single DTOF for each wavelength, in a procedure called refolding [22].

Software correction of the Differential Non-Linearity (DNL) of the TDC time scale was also required, as discussed in the following.

2.2. *In vivo* test-driven instrument upgrade

The mechanical structure, light injection path and SiPM probe described in Section 2.1 were not affected by the upgrades, which only involved the signal processing and acquisition electronics. Specifically, *in vivo* measurements led to the replacement of the SC-TDC with the 8-channel MultiHarp 150 8N from PicoQuant (Germany [36]), which became available in April 2019. The use of the MultiHarp (MH) device also allowed the removal of the LVTTL translation stage (Fig. 1, bottom), since the software setting of an input threshold is sufficient to recognize the incoming signal properly.

The single acquisition time is still 25 ms, but, due to different processing modalities and longer processing times of the MH (of the order of the chosen acquisition time, 25 ms, while the SC-TDC latency was on average 3 ms), the measurement step was doubled to 2 mm. This

Biomedical Optics EXPRESS

guarantees comparable total scan duration as with the SC-TDC, still without limiting the spatial resolution of the acquired images due to the intrinsic limits of diffuse optics.

2.3. Performance assessment protocols: BIP and MEDPHOT

The first step of the instrument characterization is carried out at a laboratory level by means of two performance assessment protocols: BIP (Basic Instrumental Performance) [28] and MEDPHOT [29]. They identify a few essential assays to investigate the key features of diffuse optics instruments and require the implementation of point measurements on reference solid phantoms, namely a phantom calibrated in attenuation and a set of 32 phantoms spanning a wide range of optical properties. These standardized procedures allow one to compare the two versions of the optical mammograph in terms of measurements outcomes rather than hardware specifications. The phantom set is made of resin-based homogeneous cylinders (4.5 cm height, 10.5 cm diameter) combining 4 concentrations of TiO_2 powder, as the diffusive material, with 8 different concentrations of black toner, responsible for the absorption properties, each one identified with a letter and a number, respectively. The letter stands for the nominal reduced scattering coefficient (A, B, C, D corresponding respectively to $\mu_s' = 5,\ 10,\ 15,\ 20\ \text{cm}^{-1}$) and the number indicates the nominal absorption coefficient (1, 2, 3, 4, 5, 6, 7, 8, corresponding respectively to $\mu_a = 0,\ 0.05,\ 0.10,\ 0.15,\ 0.20,\ 0.25,\ 0.30,\ 0.35\ \text{cm}^{-1}$), at 800 nm.

The full characterization of the initial set-up (Section 2.1) has already been reported elsewhere [22]. In the following, we will focus only on some of the assays, the ones that highlight the improvement of the upgrade with respect to the initial set-up and that are of major importance in view of the clinical use of the instrument. In detail, we assessed the Differential Non-Linearity (DNL) of the TDC time scale as regard the BIP protocol, the linearity, and the reproducibility in measuring homogeneous optical properties for the MEDPHOT protocol.

- *DNL* represents the non-uniformity of the time channel width in a time-correlated single-photon counting (TCSPC) system, which, in the case of the optical mammograph, is a TDC. The DNL is recorded as the response to a continuous signal produced by a battery-powered light source. Ideally, photon counts in all time channels should be identical (except for the Poisson noise). The deviation from this behavior is evaluated in terms of peak-to-peak difference normalized to the mean value:

$$\varepsilon_{DNL} = \frac{N_{DNL,max} - N_{DNL,min}}{\overline{N_{DNL}}} \tag{1}$$

- *Linearity* illustrates the dependence of the measured optical properties (μ_a and μ_s') against the conventionally true absorption and reduced scattering coefficients, for a total of four linearity plots. Conventionally true values derive from a set of previous measures performed in optimal conditions with independent set-ups.

- *Reproducibility* requires the repetition of a measurement on the same phantom under the same experimental conditions on different days.

2.4. In vivo tests

Following a TRL methodological approach, after point measurements on reference phantoms, *in vivo* measurements were performed with both instrument versions on 3 healthy women, with the approval of the Ethical Committee of Politecnico di Milano and following written informed consent. The goal of these *in vivo* measurements was to test: the extension of the scanned area compared to the actual compressed breast; the reproducibility over repeated measurements; the consistency of optically derived data with physiologic information on breast tissue. Considering that the purpose of the tests is the validation of the instrument set-up only and not of the technique, a limited number of subjects was deemed as sufficient.

Biomedical Optics EXPRESS

Scans were performed on both breasts (right, R, and left, L) and in two views (CC and OB). After the breast placement in the compression unit, the free surface of the lower plate is shielded with a black cloth, in order to avoid undesired reflections and light guiding that may cause artifacts [34] and to ensure that the probe scans only the breast volume, thus preventing needless acquisitions and the consequent increase in the overall scan time. During the measurement, the room is illuminated only by green light, so to avoid interference with the red and near-infrared laser light emitted and collected by the instrument. The Instrument Response Function (IRF) is acquired by measuring the DTOF transmitted through a Teflon sample placed between the mammograph plates set as close as possible to each other. Before each acquisition, the breast profile is outlined on transparent paper just after breast positioning and compression, thus highlighting the actual borders of the breast and of the contact area. This is useful to compare the resulting scan with the actual extension of the compressed breast.

Each volunteer underwent 3 measurement sessions on different days within one week to minimize the effects of the menstrual cycle and more generally of any physiological changes in the breast.

2.5. Data analysis

Time domain multi-wavelength data from the optical mammograph are analyzed with a fitting procedure based on the use of the homogeneous diffusion model for photon migration in turbid media under the Extrapolated Boundary Conditions [37]. The compressed breast is modelled as an infinite slab. The use of the homogeneous model allows us to retrieve the optical properties of the tissue averaged over the light path. The difference between the 7 experimental curves (one for each wavelength) and the corresponding 7 convolutions between IRF and theoretical DTOF is minimized employing the Levenberg-Marquardt algorithm [38]. The parameters of interest are μ_a and μ_s' as optical properties, oxy and deoxy-hemoglobin, water, lipids and collagen as chromophores (*i.e.* tissue constituents), a and b as scattering parameters.

The chromophore concentrations and scattering parameters are derived exploiting the spectral relation of the absorption and reduced scattering coefficients with the Beer law and the Mie theory, respectively:

$$\mu_a(\lambda) = \sum_i \varepsilon_i(\lambda) C_i \tag{2}$$

$$\mu_s'(\lambda) = a \left(\frac{\lambda}{\lambda_0}\right)^{-b} \tag{3}$$

where λ is the wavelength, $\varepsilon_i(\lambda)$ the extinction coefficient and C_i the concentration of the i^{th} chromophore; b is the scattering slope, related to the size of the scattering centers, a is the scattering amplitude, related to their density, $\lambda_0 = 600\ nm$ [39,40].

Even though chromophore concentrations and scattering parameters could be retrieved in a 2-step procedure, a global fitting procedure that employs all the wavelengths at once, in a "spectral approach", is preferable. In fact, by expressing μ_a and μ_s' in the diffusion equation directly using the above relations Eq. (2) and (3), the number of unknowns reduces, thus improving robustness and stability of the results [41,42]. Repeating these procedures for all measurement points, bidimensional spatial distributions of the chromophore concentrations and scattering parameters of the scanned breast area are produced.

For each volunteer and session, a Region Of Interest (ROI) is delimited and identically applied to all bidimensional maps to estimate average values. Two ROI selection methods are employed with different purposes:

- *Composition-based method*: a rectangular ROI is manually demarcated, small enough to enclose an area of homogeneous composition. This method depends on the operator's choice, but allows one to compare local areas.

Biomedical Optics EXPRESS

- *Barycenter-based method*: a reference area is automatically defined by maintaining only those transmittance curves whose barycenter is greater than or equal to the median of the barycenters of all the transmittance curves. This way, the ROI choice is unambiguous and excludes boundaries, where the breast is not in contact with the compression plates.

Then, the CV over the 3 sessions is computed in order to evaluate reproducibility.

3. Results and discussion

3.1. Goals of in vivo measurements

The preliminary measurements on the 3 healthy women aim at testing: the instrument ability to scan wholly and only the breast area; the reproducibility of measurements performed on close days; the consistency of the optical information with breast physiology.

The ability to scan efficiently the breast area depends both on the instrument and on the breast variability, which emerges both at intra-subject and inter-subject level. Thus, the optical mammograph must be able to adapt to all possible scenarios, depending on breast composition, size and thickness.

The instrument reproducibility plays a fundamental role in longitudinal studies (such as the one in which the instrument is currently enrolled), because optical data must be sensitive to changes in breast composition over time. In the preliminary *in vivo* tests, the average of chromophore concentrations and optical properties were computed over a large portion of the breast (within ROIs defined with the barycentre-based method, as defined in Section 2.5). The variation of the averages over different sessions was expressed in terms of CV, where a low CV indicates that the measurement is reproducible.

Finally, optically derived parameters were averaged over local areas as well as the entire breast to check whether the results are compatible with known information on the breast physiology.

3.2. Stages of the instrumental upgrade

The validation of the optical mammograph for NAC monitoring, including the sequence of point measurements on phantoms, scans of a breast-shaped phantom, and *in vivo* tests, was performed first on the initial architecture (Section 2.1), thus highlighting its limitations, and then repeated after the upgrade (Section 2.2) made to remove them.

The full results of the BIP and MEDPHOT protocols obtained on the initial instrument set-up have already been described previously [22]. They proved the quality of the new detection chain, composed by the combination of SiPMs and TDC, provided that refolding of the time scale and DNL correction were implemented to compensate for the SC model limits.

After the characterization with point measurements, scans were obtained on a breast-shaped silicone phantom (as the one represented in Fig. 2). The scan correctly covered the whole phantom extension without exceeding its borders. The good quality of the scan, combined with previous positive results, suggested that the optical mammograph was ready for *in vivo* tests.

The key limitations we encountered when moving from laboratory to *in vivo* validation were: 1) insufficient dynamic range in the acquisition set-up causing the system to saturate across the breast scan for some breast types due to reduced thickness at the borders (see Section 3.4); 2) high day-by-day variability in the retrieved tissue composition; 3) in some cases, inconsistency of the retrieved breast composition with respect to independent information available on breast tissue. These limitations emerged only during the *in vivo* tests, implying that the BIP and MEDPHOT standardized protocols are important to reach a validation at a laboratory level (TRL4), but they alone are not enough to fully assess the instrument performance under *in vivo* conditions towards accomplishment of TRL5.

The specific aspects will be discussed in the following (Section 3.4), for easier comparison of results achieved with the SC-TDC and MH.

Biomedical Optics EXPRESS

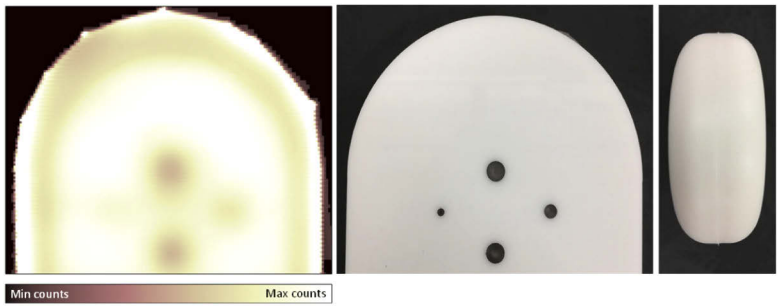

Fig. 2. Total count rate image (left) resulting from the scan of a breast-shaped silicone phantom performed with the initial instrument set-up. The phantom is composed of two specular parts, which need to be perfectly overlapped. Four totally absorbing inclusions of different sizes are localized in a slice, flush with the internal surface (center). The phantom reproduces the reduction in thickness on the borders of a compressed breast, as it can be observed from the front view (nipple point of view, right).

In light of the results we obtained, the SC model, despite being a valid TDC, proved unable to guarantee optimal performances at the conditions defined by our optical mammograph. The SC-TDC is designed mainly for high-energy physics applications and requires substantial data pre-processing when used in TD diffuse optics. It can represent a good choice for a high-throughput detection chain, but it is not suitable in our measurement conditions, as it cannot manage the wide count rate dynamics experienced over short time intervals, when the scan moves close to the border of the compressed breast. Thus, the detection chain was upgraded, still using SiPMs as detectors and a TDC for TCSPC (Section 2.2). Specifically, our demanding measurement conditions could be properly managed with a device only recently become commercially available: the MH, designed for TCSPC applications and specifically optimized to boost single-photon data throughput. The TDC replacement allowed us to improve and simplify the set-up, with the removal of the LVTTL stage. Furthermore, refolding and DNL correction are no longer needed, reducing signal manipulation. Table 2 summarizes the relevant specifications of the two TDC devices.

Table 2. Comparison between relevant SC-TDC and MH specifications[a]

Feature	SC-TDC	MH
DNL	<90%	<10%
Maximum sync rate	7 MHz	78 MHz
Maximum throughput	40 Mcps	180 Mcps
Dead time	5.5 ns	<650 ps
Price	€	€€€

[a]Nominal values reported in [43] and [22] for SC-TDC and [36] for MH.

As specified in Section 2.2, to cope with its higher latency between subsequent measurements (about 25 ms *vs* 3 ms for SC-TDC), the use of the MH implied an increase from 1 mm to 2 mm in the data acquisition step (and correspondingly in the image pixel size). However, that change does not significantly affect the imaging performances and does not introduce any relevant loss in terms of reconstructed parameters, taking into account the limited spatial resolution of diffuse optics.

Biomedical Optics EXPRESS

3.3. BIP and MEDPHOT with the new set-up

The application of the BIP and MEDPHOT protocols offered a direct way to compare the measurement outcomes of the two instrument versions. The protocols were applied for all the 7 wavelengths, but, for the sake of brevity, only findings at one representative wavelength (785 nm) will be described, where applicable.

To highlight the measured DNL, Fig. 3 shows the number of recorded photon counts normalized to the mean value as a function of the bin number, within a time window of about 4 ns to better appreciate the DNL pattern. Since any non-uniformity affects the reconstructed optical parameters, proper compensation methods must be applied in post-processing in case the DNL is too large. The SC-TDC, whose time channel width is 82.3 ps, exhibits a strong DNL (maximum $\varepsilon_{DNL} = 88\%$, computed using Eq. (1), with a periodic jigsaw pattern. The compensation algorithm we applied dramatically reduces it to a residual value of 4%. On the contrary, for the MH (time channel width equal to 80 ps), ε_{DNL} is 2% at maximum, with no need for correction strategies.

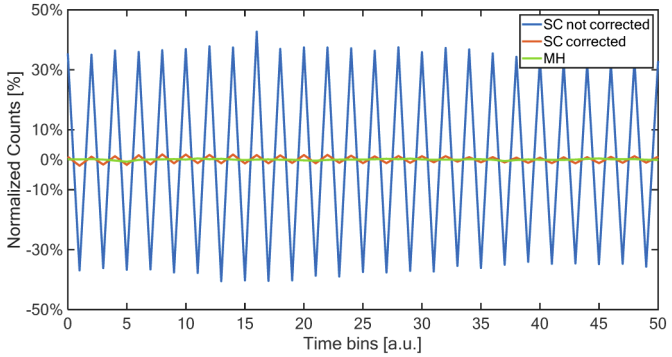

Fig. 3. Normalized counts over time bins for SC-TDC (with and without correction algorithm) and for MH.

The linearity plots illustrated in Fig. 4 and Fig. 5 are one of the outputs of the MEDPHOT protocol. Linearity investigates the relationship between nominal and measured optical properties and the coupling between absorption and scattering, which could compromise the capability of the instrument to detect changes in an optical property. Moreover, good linearity in the estimate of the absorption properties grants the correctness of the relative concentrations of the tissue constituents. In the plots shown in Fig. 5, each diamond corresponds to one of the 32 phantoms. Each combination of color (*i.e.* blue, red, green or yellow) and symbol (*i.e.* full or empty diamond) corresponds to a specific letter (A, B, C, D) or number (1, 2, 3, 4, 5, 6, 7, 8) sequence. Letter (number) sequences represent increasing values of the conventionally true reduced scattering (absorption) coefficient. Straight lines derive from the linear interpolation based on the first 4 values of a sequence. Line slopes are compared in terms of angular coefficient m. By comparison with the linearity plots obtained with the SC-TDC set-up carried out at the beginning of the validation process (Fig. 4), a slight, but not negligible overall improvement of the performances can be observed using the MH (Fig. 5), which is very beneficial for a longitudinal study. The results for a single wavelength (785 nm) are reported, since it is representative of all the others (see Supplementary Material).

Figure 5(a) illustrates the reconstructed absorption coefficient with respect to the nominal one. It reveals a good linearity of the measured absorption properties, with an improvement especially on series A (corresponding to $\mu_s' = 5$ cm^{-1}) with respect to the SC counterparts (the ideal angular coefficient is $m_{ideal} = 1$ and experimentally we obtain $m_{MH_{A,abs}} = 1.13$ *vs* $m_{SC_{A,\,abs}} = 1.24$).

The improvement is even clearer in Fig. 5(b), showing the reconstructed absorption coefficient *vs* the nominal scattering coefficient, thus highlighting the absorption-to-scattering coupling.

Biomedical Optics EXPRESS

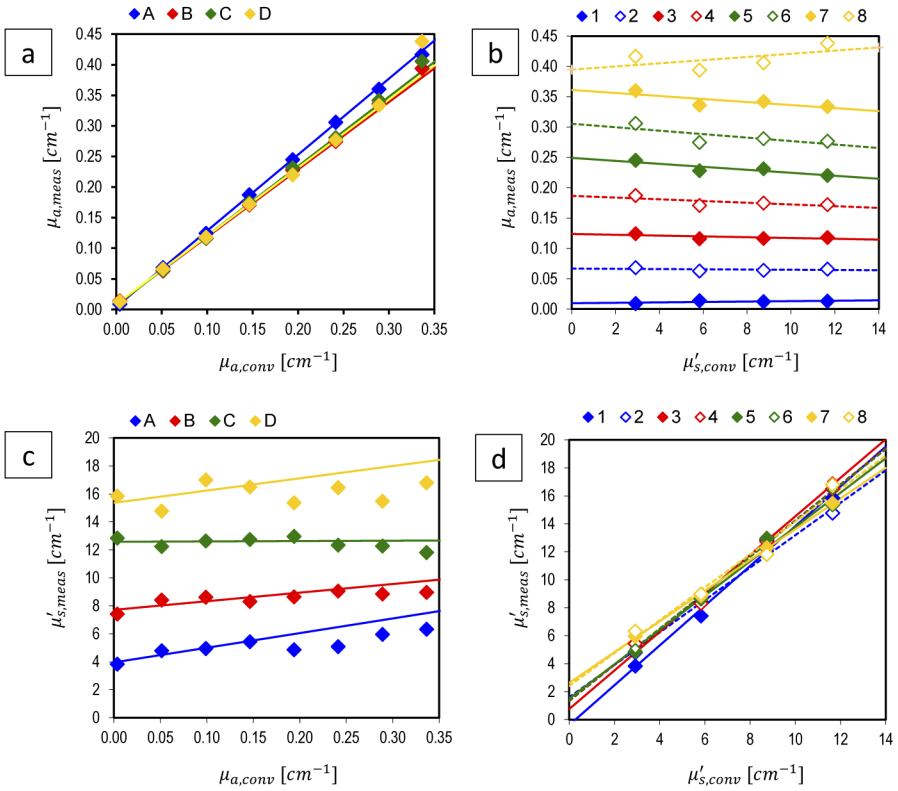

Fig. 4. Linearity plots for the upgraded SC-TDC-based mammograph at 785 nm: a) measured absorption *vs* nominal absorption; b) measured absorption-to-scattering coupling; c) measured scattering *vs* nominal scattering; d) measured scattering-to-absorption coupling.

The coupling is now totally negligible: the lines are fairly horizontal (the ideal angular coefficient should be null), with an average angular coefficient for series 1 to 7 equal to $m_{MH_{av,1-7}} = 6.9\times10^{-4}$. An exception occurs for the phantoms with highest absorption (series 8: $\mu_a = 0.35$ cm^{-1}, corresponding to the yellow line with empty diamonds), for which a slight positive coupling arises ($m_{MH_8} = 3.8\times10^{-3}$). The same plot for the SC-TDC shows generally higher slopes, *e.g.* an angular coefficient 4 times larger for series 4 and 5, which reveals absorption-to-scattering coupling.

Figure 5(c) displays the reconstructed scattering coefficient *vs* the nominal absorption coefficient. The new set-up results indicate a smaller scattering-to-absorption coupling for low scattering values. In fact, the variation of the measured μ_s' along the x axis for the A series ($m_{MH_{A,sca}} = 2.74$) is now about half compared to the SC-TDC case ($m_{SCA,sca} = 5.82$), while the B ($\mu'_s = 10\ cm^{-1}$, in red) and C ($\mu'_s = 15\ cm^{-1}$, in green) series show results similar to the previous configuration. The D series ($\mu'_s = 20\ cm^{-1}$, in yellow), on the contrary, exhibits now a steeper trend line ($m_{MH_D} = 17.46$ *vs* $m_{SCD} = 8.81$). However, the angular coefficients reduce if we consider all the 8 data points rather than the first 4, but the MH value remains higher than the SC-TDC counterpart ($m_{MH_D} = 7.09$ *vs* $m_{SCD} = 1.85$).

Finally, Fig. 5(d) shows the reconstructed reduced scattering coefficient *vs* the nominal one. With respect to the SC-TDC-based outcomes, the intercept values of lines are now smaller (the average value for the new set-up is $q_{MH,av} = 0.48\ cm^{-1}$, while for the initial one it is $q_{SC,av} = 1.40\ cm^{-1}$).

Biomedical Optics EXPRESS

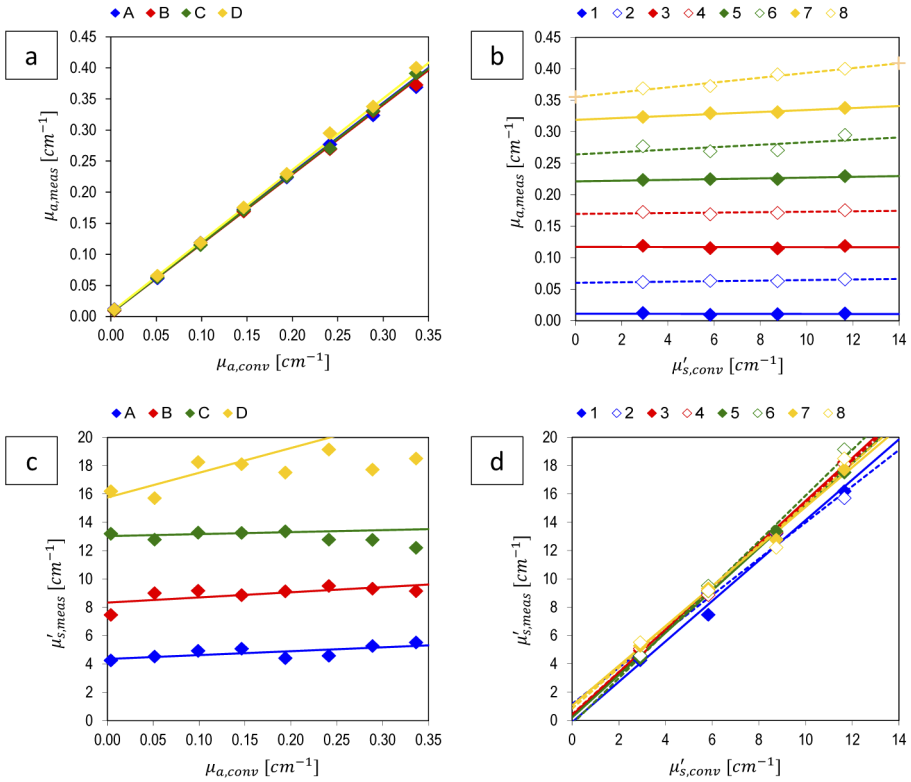

Fig. 5. Linearity plots for the upgraded MH-based mammograph at 785 nm.

In general, better results are obtained for the absorption coefficient (Fig. 5(a) and Fig. 5(b), maximum angular coefficient deviation from ideal behaviour equal to $\Delta m_{MH_{abs}} = 0.15$) rather than for scattering (Fig. 5(c) and Fig. 5(d), $\Delta m_{MH_{sca}} = 6.09$).

Figure 6 shows the results for the reproducibility assay. It examines the instrument reliability and self-consistency over time, which is particularly important for clinical studies, both transversal and longitudinal ones, to correctly investigate differences among subjects measured at different times and changes over time in the same subject, respectively. The absorption and the reduced scattering coefficient of a specific phantom (B2: $\mu_a = 0.05\ cm^{-1}$, $\mu'_s = 10\ cm^{-1}$) were measured on 3 different days and the variations $\Delta\mu_a$ and $\Delta\mu_s'$ with respect to the mean were computed (*i.e.* the 0% horizontal line in Fig. 6). As regard the SC-TDC, variations of the optical properties remain within ± 3%. At $\lambda = 785$ nm, the CV is 1.3% for μ_a and 2.4% for μ_s'. As regards the MH, variations are smaller than 1%, with a CV of 0.62% for μ_a and 0.65% for μ_s'. Fluctuations of the measured optical properties on phantoms, then, are negligible in both cases, as compared to intra- and inter-subject variability expected for *in vivo* measurements.

3.4. *In vivo measurements with the new set-up*

The study on the same 3 healthy volunteers as considered previously was repeated on the upgraded set-up, maintaining the same protocol and data analysis method.

The first immediate achievement is the extension of the scanned area. Figure 7 reports the same breast and view scanned at different times with the two set-ups. The increase in output count rate caused by the thickness reduction at breast borders overcame the SC-TDC maximum throughput, thus strongly limiting the imaged area and not allowing a complete breast scan with

Biomedical Optics EXPRESS

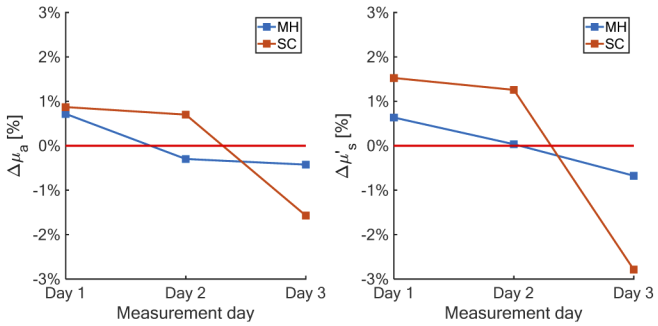

Fig. 6. Reproducibility plots for SC-TDC and MH: variation in absorption coefficient (left) and reduced scattering coefficient (right) over different days.

the previous set-up (Fig. 7(a)). Instead, now (Fig. 7(b)) the projection portrays the whole breast, including the portion not in direct contact with the glass plates of the compression unit, thanks to the much higher maximum throughput of the MH, never reached during measurements. That is the reason why the breast boundary is also smoother. In a clinical setting, it is important to probe the whole breast area, since tumors could potentially be located also in the peripheral area. The core of the image with the breast in contact (dashed red line) looks darker as compared to Fig. 7(a) simply because the full-scale range of the image is now polarized by the higher counts on the border.

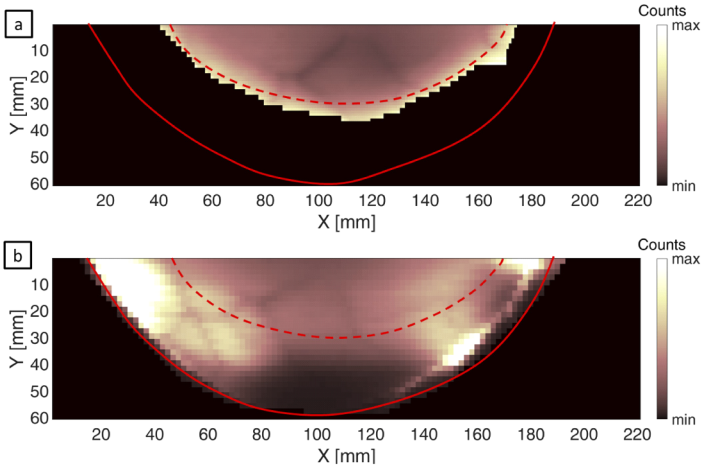

Fig. 7. Count rate image, obtained summing all wavelengths and all detectors contributions, of the same CC R view acquired with the SC-TDC (a) and MH (b). The red curves highlight the actual borders of the breast (solid line) and the extension of the contact area (dashed line).

To quantify the improvement in terms of dynamic range, we computed the ratio between the maximum (reached at the border of the breast) and minimum (when no photons arrived at the detector, thus recording only dark count noise) overall count rates obtained during the scan for each image, summing up information from all wavelengths and all detectors. The maximum count rate successfully recorded with the SC-TDC (MH) is 39.373 M (161.686 M) counts per second (cps). In both cases, the contribution of dark counts is 700 kcps, thus resulting into a dynamic range of 56.25 (230.98) with the SC-TDC (MH). It is therefore clear that the extended

Biomedical Optics EXPRESS

imaging capability observed when using the MH is strongly linked to the increase in the dynamic range by more than a factor of 4.

In order to assess the consistency of optical data with the breast structure, the average composition was estimated in different areas within the same breast and compared with independent information. The mammary gland is composed of fibro-glandular tissue, mainly localized in the outer quadrants. Then, higher concentration of water and collagen and lower content of lipids are expected with respect to adipose tissue (inner quadrants). Figure 8 shows an example of the two ROIs used to evaluate the composition of the mammary gland (red, outer quadrant) with respect to the adipose tissue (blue, inner quadrant). To support the different composition expected in the two areas, the corresponding x-ray image is also reported.

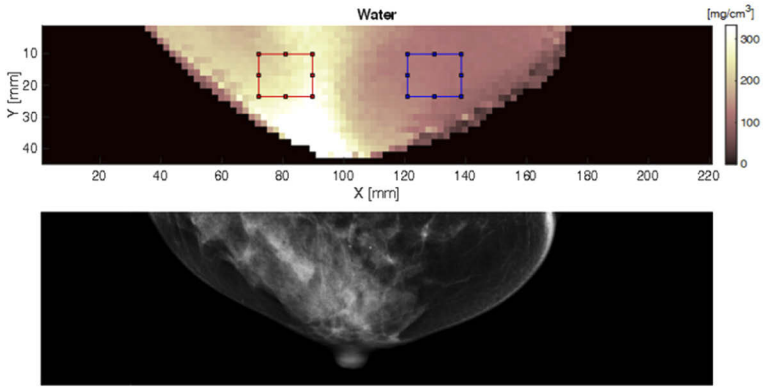

Fig. 8. Water map of subject #2 (a) and corresponding x-ray mammogram (b), CC R view. The red and blue rectangles identify the composition-based ROIs selected as representative of the outer and inner quadrant, respectively.

Table 3 reports water, collagen and lipids content in the external and internal quadrants (CC R view) of the 3 subjects averaged over the 3 measurement sessions. Expectations are confirmed for all volunteers. These results indicate that the optical information is sensitive to the breast composition and will hopefully allow us to track its changes over time.

Table 3. Tissue composition (water, collagen and lipids) in the outer and inner quadrants averaged over the 3 measurement sessions.

	Subject #1		Subject #2		Subject #3	
Component	Outer	Inner	Outer	Inner	Outer	Inner
Water [mg/cm^3]	333	240	201	117	231	183
Collagen [mg/cm^3]	96.6	55.4	83.7	34.6	32.4	22.7
Lipids [mg/cm^3]	524	643	661	758	695	740

Table 4, Table 5 and Table 6 report the complete data set obtained from the CC R and L views of the 3 subjects with the upgraded optical mammograph. Mean chromophore concentrations and scattering parameters were derived applying the barycenter-based ROI selection method. CV values obtained for both the initial (CV_{SC}) and the new (CV_{MH}) configurations are reported. The last two columns ((R - L)/R) list the percentage difference in mean value for each chromophore between R and L breasts, normalized to R values. Once again, the comparison between contralateral breasts was carried out for both the instrument versions.

In Table 4, the CV for subject #1 ranges from 1% to 9% over the 3 sessions (*vs* 3% to 43% with the SC-TDC counterpart), while Table 5, dedicated to subject #2, shows a maximum CV equal to 10% (*vs* 42%) for the right breast and 13% for the left one (*vs* 33%). In Table 6 (subject #3), the

Biomedical Optics EXPRESS

Table 4. Average values of chromophore concentrations derived with the barycenter-based ROI selection method in the 3 measurement sessions with the new set-up on subject #1 (CC R and L views). CVs and comparison between contralateral breasts are provided for both set-up versions[a]

	Right breast					Left breast						
	Session			CV		Session			CV		(R - L)/R	
Parameter	1	2	3	SC	MH	1	2	3	SC	MH	SC	MH
a	14.0	13.5	13.7	17	2	13.8	13.7	13.5	11	1	0	0
b	0.71	0.69	0.69	12	2	0.67	0.65	0.61	17	5	23	8
Water	293	301	302	7	2	278	291	280	3	3	−6	5
Collagen	72	77	79	43	4	69	78	80	29	8	−21	0
Lipids	588	560	561	5	3	592	571	603	7	3	−5	−3
HbT	17	17	15	7	9	16	16	14	5	8	1	6
SO_2	73	72	69	10	3	70	73	70	9	2	−11	0

Table 5. Average values of chromophore concentrations derived with the barycenter-based ROI selection method in the 3 measurement sessions with the new set-up on subject #2 (CC R and L views). CVs and comparison between contralateral breasts are provided for both set-up versions[a]

	Right breast					Left breast						
	Session			CV		Session			CV		(R - L)/R	
Parameter	1	2	3	SC	MH	1	2	3	SC	MH	SC	MH
a	11.3	11.6	11.2	2	2	10.2	9.9	10.7	11	4	2	10
b	0.85	0.77	0.95	16	10	0.93	0.78	0.74	18	12	22	5
Water	198	181	180	8	6	180	168	178	6	4	15	6
Collagen	58	57	53	42	5	42	52	53	33	12	−29	13
Lipids	674	671	697	2	2	599	670	637	8	6	−1	7
HbT	8	8	7	10	6	12	10	9	15	13	−31	−35
SO_2	63	69	58	17	8	66	68	62	3	5	−26	−3

Table 6. Average values of chromophore concentrations derived with the barycenter-based ROI selection method in the 3 measurement sessions with the new set-up on subject #3 (CC R and L views). CVs and comparison between contralateral breasts are provided for both set-up versions[a]

	Right breast					Left breast						
	Session			CV		Session			CV		(R - L)/R	
Parameter	1	2	3	SC	MH	1	2	3	SC	MH	SC	MH
a	13.8	13.4	13.7	1	1	14.3	13.8	13.8	6	2	−10	−2
b	0.65	0.61	0.75	23	11	0.63	0.50	0.64	11	13	25	12
Water	199	204	209	5	2	195	199	207	6	3	3	2
Collagen	28	31	13	96	41	27	35	16	45	37	−54	−8
Lipids	726	716	677	3	4	729	725	703	1	2	−3	−2
HbT	18	17	16	19	6	17	17	17	20	2	3	0
SO_2	77	73	69	8	5	75	76	72	8	3	−1	−2

[a] a [cm^{-1}], b adimentional, water, collagen and lipids [mg/cm^3], HbT [μM], SO_2 [%], CV [%], (R - L)/R [%].

Biomedical Optics EXPRESS

CV for all parameters never exceeds 13% (*vs* 23%), except for collagen. The high variability observed on collagen may be at least partly attributed to its concentration (which is particularly low in this subject) and its low specific absorption, yielding to a contribution to the overall tissue absorption that is small and consequently difficult to accurately quantify. Furthermore, the large CV is caused by a drop in collagen content estimated in the third session. Since it occurs in both breasts (R and L) and in both views (CC and OB), it might at least in part be attributed to physiological changes related to the menstrual cycle. Specifically, data collected on subject 3 in session 3 show some increase in the estimated water content, which may correspond to tissue swelling and overall reduction in the density of other constituents. Finally, the percentage comparison between mean values of R and L breasts confirms the improvement achieved with the MH-based set-up and reveals overall small differences after the upgrade. The largest percentage variations are related to the parameters described by small numbers. Such variations are in line with the CVs obtained over sessions and could be due to the fact that contralateral breasts are never perfectly identical.

These data suggest an acceptable level of reproducibility for the clinical trial. Such an improvement is mainly due to the reduced signal manipulation (no DNL correction nor refolding) and depends only marginally on the larger extension of the probed breast area (that in principle could better average over tissue heterogeneity). Moreover, the similar results obtained for the right and left breast support the hypothesis of data consistency, already made based on the comparison between outer and inner quadrants.

Table 7 reports the mean values and the CV over sessions for each parameter, comparing CC R and OB R views for all participants. CC and OB views show very similar results, especially as regard the main constituents of breast tissue: water and lipids. The percentage difference of their CC and corresponding OB averages is never larger than 2% (at maximum 8 mg/cm^3) and their CV over sessions ranges from 1% to 6%. Collagen and hemoglobin are generally higher in the OB view than the CC counterpart, probably because it probes a larger portion of fibro-glandular tissue. However, these parameters also show higher variability than the two major constituents. The comparison confirms that collagen is the component with the highest fluctuations when its concentration is low (CV equal to 41% for CC and 26% for OB in subject #3), followed by the *b* parameter. In fact, collagen and *b* are both linked to the scattering properties of the tissue, for which also the linearity test of the MEDPHOT protocol registers higher variability with respect to absorption. Still with reference to the reproducibility assay of the MEDPHOT protocol, *in vivo* measurements report larger CV values than phantom measurements (below 1%), but this was expected due to the intrinsic heterogeneity and variability over time of the breast tissue.

Table 7. Mean values (Avg) and CVs of chromophores concentrations and scattering parameters for each subject, over the three sessions with the new set-up. CC R and OB R views [a]

	Subject #1				Subject #2				Subject #3			
	CC		OB		CC		OB		CC		OB	
Parameter	Avg	CV	Avg	CV	Avg	CV	Avg	CV	Avg	CV	Avg	CV
a	13.7	2	12.8	5	11.4	2	10.9	4	13.6	1	12.3	6
b	0.70	2	0.71	9	0.86	10	0.66	12	0.67	11	0.59	24
Water	299	2	300	1	186	6	182	3	204	2	208	2
Collagen	76	4	82	5	56	5	69	9	24	41	58	26
Lipids	570	3	564	3	681	2	685	2	706	4	698	4
HbT	16	9	17	9	8	6	9	15	17	6	20	7
SO_2	71	3	68	1	63	8	68	1	73	5	80	6

[a] a [cm^{-1}], b adimentional, water, collagen and lipids [mg/cm^3], HbT [μM], SO_2 [%], CV [%].

Biomedical Optics EXPRESS

4. Conclusion

This paper presented the characterization of a further upgraded version of the time domain multi-wavelength optical mammograph developed by Politecnico di Milano. The tests followed a growing complexity: from standardized protocols on phantoms, to measurements on a breast-shaped phantom up to *in vivo* measurements on volunteers.

The same *in vivo* measurements performed on a previously upgraded version (exploiting a multi-SiPM detection probe and a multi-channel TDC for data acquisition) highlighted limitations that had not emerged during extensive laboratory tests, and led to the replacement of the TDC. The new model demonstrated improved performances in time domain diffuse optics, stemming from ongoing technological advancements in the field. Specifically, the new set-up features good consistency between optically derived parameters and breast physiology and improved linearity and reproducibility of the retrieved optical properties, which will hopefully allow us to monitor longitudinal changes in tissue composition during chemotherapy.

This experience also pointed out how important is a thorough characterization of instruments developed for *in vivo* studies, where laboratory conditions ensure reproducibility and comparability, but only *in vivo* tests on healthy volunteers can effectively investigate the performance in real measurement conditions, as some aspects cannot be replicated in laboratory.

Following satisfactory characterization, the instrument has now started a clinical trial on the optical monitoring of neoadjuvant chemotherapy.

Funding. Horizon 2020 Framework Programme (731877).

Disclosures. The authors declare no conflicts of interest.

Supplemental document. See Supplement 1 for supporting content.

References

1. "Cancer Facts and Figures 2020," [Online]. Available at: https://www.cancer.org/research/cancer-facts-statistics/all-cancer-facts-figures/cancer-facts-figures-2020.html, Accessed: 31/Aug./2020 (2020).
2. H. Li, L. Yao, P. Jin, L. Hu, X. Li, T. Guo, and K. Yang, "MRI and PET/CT for evaluation of the pathological response to neoadjuvant chemotherapy in breast cancer: A systematic review and meta-analysis," The Breast **40**, 106–115 (2018).
3. P. Taroni, "Diffuse optical imaging and spectroscopy of the breast: A brief outline of history and perspectives," Photochem. Photobiol. Sci. **11**(2), 241–250 (2012).
4. D. Grosenick, H. H. Rinneberg, R. Cubeddu, and P. Taroni, "Review of optical breast imaging and spectroscopy," J. Biomed. Opt. **21**(9), 091311 (2016).
5. T. Durduran, R. Choe, W. Baker, and A. G. Yodh, "Diffuse optics for tissue monitoring and tomography," Rep. Prog. Phys. **73**(7), 076701 (2010).
6. D. R. Busch, R. Choe, T. Durduran, and A. G. Yodh, "Toward noninvasive characterization of breast cancer and cancer metabolism with diffuse optics," PET Clinics **8**(3), 345–365 (2013).
7. R. Choe and T. Durduran, "Diffuse optical monitoring of the neoadjuvant breast cancer therapy," IEEE J. Sel. Top. Quantum Electron. **18**(4), 1367–1386 (2012).
8. P. Taroni, A. Pifferi, G. Quarto, L. Spinelli, A. Torricelli, F. Abbate, A. Villa, N. Balestreri, S. Menna, E. Cassano, and R. Cubeddu, "Noninvasive assessment of breast cancer risk using time-resolved diffuse optical spectroscopy," J. Biomed. Opt. **15**(6), 060501 (2010).
9. P. Taroni, G. Quarto, A. Pifferi, F. Ieva, A. M. Paganoni, F. Abbate, N. Balestreri, S. Menna, E. Cassano, and R. Cubeddu, "Optical identification of subjects at high risk for developing breast cancer," J. Biomed. Opt. **18**(6), 060507 (2013).
10. P. Taroni, A. Torricelli, L. Spinelli, A. Pifferi, F. Arpaia, G. Danesini, and R. Cubeddu, "Time-resolved optical mammography between 637 and 985 nm: Clinical study on the detection and identification of breast lesions," Phys. Med. Biol. **50**(11), 2469–2488 (2005).
11. G. Quarto, L. Spinelli, A. Pifferi, A. Torricelli, R. Cubeddu, F. Abbate, N. Balestreri, S. Menna, E. Cassano, and P. Taroni, "Estimate of tissue composition in malignant and benign breast lesions by time-domain optical mammography," Biomed. Opt. Express **5**(10), 3684 (2014).
12. A. Farina, S. Konugolu Venkata Sekar, C. Guadagno, L. Spinelli, P. Lanka, P. Taroni, R. Cubeddu, E. Nisoli, and A. Pifferi, "In vivo depth heterogeneity of the abdomen assessed by broadband time-domain diffuse optical spectroscopy," in *Diffuse Optical Spectroscopy and Imaging VI*, H. Dehghani and H. Wabnitz, eds. (SPIE, 2017), Part F61-E, p. 39.
13. B. J. Tromberg, Z. Zhang, A. Leproux, T. D. O'Sullivan, A. E. Cerussi, P. M. Carpenter, R. S. Mehta, D. Roblyer, W. Yang, K. D. Paulsen, B. W. Pogue, S. Jiang, P. A. Kaufman, A. G. Yodh, S. H. Chung, M. Schnall, B. S. Snyder, N.

Biomedical Optics EXPRESS

Hylton, D. A. Boas, S. A. Carp, S. J. Isakoff, and D. Mankoff, "Predicting responses to neoadjuvant chemotherapy in breast cancer: ACRIN 6691 trial of diffuse optical spectroscopic imaging," Cancer Res. **76**(20), 5933–5944 (2016).
14. F. Bevilacqua, A. J. Berger, A. E. Cerussi, D. Jakubowski, and B. J. Tromberg, "Broadband absorption spectroscopy in turbid media by combined frequency-domain and steady-state methods," Appl. Opt. **39**(34), 6498 (2000).
15. Q. Zhu, S. Tannenbaum, S. H. Kurtzman, P. DeFusco, A. Ricci, H. Vavadi, F. Zhou, C. Xu, A. Merkulov, P. Hegde, M. Kane, L. Wang, and K. Sabbath, "Identifying an early treatment window for predicting breast cancer response to neoadjuvant chemotherapy using immunohistopathology and hemoglobin parameters," Breast Cancer Res. **20**(1), 1–17 (2018).
16. C. Xu, H. Vavadi, A. Merkulov, H. Li, M. Erfanzadeh, A. Mostafa, Y. Gong, H. Salehi, S. Tannenbaum, and Q. Zhu, "Ultrasound-guided diffuse optical tomography for predicting and monitoring neoadjuvant chemotherapy of breast cancers," Ultrason Imaging **38**(1), 5–18 (2016).
17. S. Jiang, B. W. Pogue, P. A. Kaufman, J. Gui, M. Jermyn, T. E. Frazee, S. P. Poplack, R. DiFlorio-Alexander, W. A. Wells, and K. D. Paulsen, "Predicting breast tumor response to neoadjuvant chemotherapy with diffuse optical spectroscopic tomography prior to treatment," Clin. Cancer Res. **20**(23), 6006–6015 (2014).
18. S. Jiang, B. W. Pogue, C. M. Carpenter, S. P. Poplack, W. A. Wells, C. A. Kogel, J. A. Forero, L. S. Muffly, G. N. Schwartz, K. D. Paulsen, and P. A. Kaufman, "Evaluation of breast tumor response to neoadjuvant chemotherapy with tomographic diffuse optical spectroscopy: Case studies of tumor region-of-interest changes," Radiology **252**(2), 551–560 (2009).
19. A. Y. Sajjadi, S. J. Isakoff, B. Deng, B. Singh, C. M. Wanyo, Q. Fang, M. C. Specht, L. Schapira, B. Moy, A. Bardia, D. A. Boas, and S. A. Carp, "Normalization of compression-induced hemodynamics in patients responding to neoadjuvant chemotherapy monitored by dynamic tomographic optical breast imaging (DTOBI)," Biomed. Opt. Express **8**(2), 555 (2017).
20. J. E. Gunther, E. A. Lim, H. K. Kim, M. L. Flexman, M. Altoé, J. A. Campbell, H. Hibshoosh, K. D. Crew, K. Kalinsky, D. L. Hershman, and A. H. Hielscher, "Dynamic Diffuse Optical Tomography for Monitoring Neoadjuvant Chemotherapy in Patients with Breast Cancer," Radiology **287**(3), 778–786 (2018).
21. M. L. Flexman, M. A. Khalil, R. Al Abdi, H. K. Kim, C. J. Fong, E. Desperito, D. L. Hershman, R. L. Barbour, and A. H. Hielscher, "Digital optical tomography system for dynamic breast imaging," J. Biomed. Opt. **16**(7), 076014 (2011).
22. E. Ferocino, E. Martinenghi, A. Dalla Mora, A. Pifferi, R. Cubeddu, and P. Taroni, "High throughput detection chain for time domain optical mammography," Biomed. Opt. Express **9**(2), 755 (2018).
23. C. Luparello, "Aspects of Collagen Changes in Breast Cancer," J. Carcinog. Mutagen. S13, (2013).
24. C. Voutouri, C. Polydorou, P. Papageorgis, V. Gkretsi, and T. Stylianopoulos, "Hyaluronan-Derived Swelling of Solid Tumors, the Contribution of Collagen and Cancer Cells, and Implications for Cancer Therapy," Neoplasia **18**(12), 732–741 (2016).
25. J. Liu, J.-X. Shen, H.-T. Wu, X.-L. Li, X.-F. Wen, C.-W. Du, and G.-J. Zhang, "Collagen 1A1 (COL1A1) promotes metastasis of breast cancer and is a potential therapeutic target," Discov. Med. **25**(139), 211–223 (2018).
26. M. Héder, "From NASA to EU: The evolution of the TRL scale in Public Sector Innovation," Innov. J. **22**(2), 1–23 (2017).
27. European Commission, "Technology readiness levels (TRL)," Horiz. 2020 – Work Program. 2014-2015 Gen. Annex. Extr. from Part 19 - Comm. Decis. C (2014), 1 (2014).
28. H. Wabnitz, D. R. Taubert, M. Mazurenka, O. Steinkellner, A. Jelzow, R. Macdonald, D. Milej, P. Sawosz, M. Kacprzak, A. Liebert, R. Cooper, J. Hebden, A. Pifferi, A. Farina, I. Bargigia, D. Contini, M. Caffini, L. Zucchelli, L. Spinelli, R. Cubeddu, and A. Torricelli, "Performance assessment of time-domain optical brain imagers, part 1: basic instrumental performance protocol," J. Biomed. Opt. **19**(8), 086010 (2014).
29. A. Pifferi, A. Torricelli, A. Bassi, P. Taroni, R. Cubeddu, H. Wabnitz, D. Grosenick, M. Möller, R. Macdonald, J. Swartling, T. Svensson, S. Andersson-Engels, R. L. P. van Veen, H. J. C. M. Sterenborg, J.-M. Tualle, H. L. Nghiem, S. Avrillier, M. Whelan, and H. Stamm, "Performance assessment of photon migration instruments: the MEDPHOT protocol," Appl. Opt. **44**(11), 2104 (2005).
30. H. Wabnitz, A. Jelzow, M. Mazurenka, O. Steinkellner, R. Macdonald, D. Milej, N. Zolek, M. Kacprzak, P. Sawosz, R. Maniewski, A. Liebert, S. Magazov, J. Hebden, F. Martelli, P. Di Ninni, G. Zaccanti, A. Torricelli, D. Contini, R. Re, L. Zucchelli, L. Spinelli, R. Cubeddu, and A. Pifferi, "Performance assessment of time-domain optical brain imagers, part 2: nEUROPt protocol," J. Biomed. Opt. **19**(8), 086012 (2014).
31. P. Lanka, L. Yang, D. Orive-Miguel, J. D. Veesa, S. Tagliabue, A. Sudakou, S. Samaei, M. Forcione, Z. Kovacsova, A. Behera, L. Hervé, T. Durduran, A. Liebert, P. Sawosz, A. Belli, I. Tachtsidis, A. Dalla Mora, H. Dehghani, H. Wabnitz, and A. Pifferi, "The BITMAP exercise: a multi-laboratory performance assessment campaign of diffuse optical instrumentation," in *Diffuse Optical Spectroscopy and Imaging VII*, H. Dehghani and H. Wabnitz, eds. (SPIE, 2019), 11074, p. 44.
32. D. Orive-Miguel, P. Lanka, L. Yang, S. Tagliabue, A. Sudakou, S. Samaei, J. D. Veesa, M. Forcione, Z. Kovacsova, A. Behera, L. Hervé, T. Durduran, A. Liebert, P. Sawosz, A. Belli, I. Tachtsidis, A. Dalla Mora, J. Mars, L. Condat, A. Torricelli, H. Dehghani, H. Wabnitz, and A. Pifferi, "The BitMap dataset: an open dataset on performance assessment of diffuse optics instruments," in *Diffuse Optical Spectroscopy and Imaging VII*, H. Dehghani and H. Wabnitz, eds. (SPIE, 2019), Part F142-, p. 45.

Biomedical Optics EXPRESS

33. "Standardisation and performance assessment in Biophotonics - Workshop report," [Online]. Available at: https://ec.europa.eu/digital-single-market/en/news/standardisation-and-performance-assessment-biophotonics-report. Accessed: 30/Aug./2020 (2020.
34. P. Taroni, A. Pifferi, E. Salvagnini, L. Spinelli, and R. Cubeddu, "Seven-wavelength time-resolved optical mammography extending beyond 1000 nm for breast collagen quantification," 17(18), 504–510 (2009).
35. Surface Concept GmbH, "SC-TDC Datasheet," [Online]. Available at: https://www.surface-concept.com/products_time.html#MCTDC, Accessed: 01/Sep./2020 2020.
36. PicoQuant GmbH, "MultiHarp 150 Datasheet," [Online]. Available at: https://www.picoquant.com/products/category/tcspc-and-time-tagging-modules/multiharp-150-high-throughput-multichannel-event-timer-tcspc-unit, Accessed: 01/Sep./2020 (2020).
37. F. Martelli, S. Del Bianco, A. Ismaelli, and G. Zaccanti, *Light Propagation through Biological Tissue and Other Diffusive Media: Theory, Solutions, and Software* (SPIE, 2009).
38. W. H. Press, S. A. Teukolsky, W. T. Vetterling, and B. P. Flannery, *Numerical Recipes in C: The Art of Scientific Computing* (Cambridge University Press, 2002).
39. X. Wang, B. W. Pogue, S. Jiang, X. Song, K. D. Paulsen, C. A. Kogel, S. P. Poplack, and W. A. Wells, "Approximation of Mie scattering parameters in near-infrared tomography of normal breast tissue in vivo," J. Biomed. Opt. **10**(5), 051704 (2005).
40. J. R. Mourant, T. Fuselier, J. Boyer, T. M. Johnson, and I. J. Bigio, "Predictions and measurements of scattering and absorption over broad wavelength ranges in tissue phantoms," Appl. Opt. **36**(4), 949 (1997).
41. C. D'Andrea, L. Spinelli, A. Bassi, A. Giusto, D. Contini, J. Swartling, A. Torricelli, and R. Cubeddu, "Time-resolved spectrally constrained method for the quantification of chromophore concentrations and scattering parameters in diffusing media," Opt. Express **14**(5), 1888 (2006).
42. A. Farina, A. Bassi, A. Pifferi, P. Taroni, D. Comelli, L. Spinelli, and R. Cubeddu, "Bandpass Effects in Time-Resolved Diffuse Spectroscopy," Appl. Spectrosc. **63**(1), 48–56 (2009).
43. Surface Concept GmbH, "Time-to-Digital Converters (TDCs) Features / Specifications," [Online]. Available at: https://www.surface-concept.com/downloads/info/Datasheet_TDC.pdf. Accessed: 30/Aug./2020.

93.56.170.208 {ts '2021-01-27 11:45:10'}